Analysis and control of Hall effect thruster using optical emission spectroscopy and artificial neural network

Tarek Ben Slimane, Alexandre Leduc, Loïc Schiesko, Anne Bourdon, Pascal Chabert

Analysis and Control of Hall Effect Thruster using Optical Emission Spectroscopy and Artificial Neural Network

Tarek Ben Slimane,[1] Alexandre Leduc,[1] Loic Schiesko,[1] Anne Bourdon,[1] and Pascal Chabert[1]

Laboratoire de Physique des Plasmas (LPP), CNRS, Sorbonne Université, École Polytechnique, Institut Polytechnique de Paris, 91120 Palaiseau, France

(*tarek.ben-slimane@polytechnique.org)

(Dated: 19 September 2024)

This study presents a proof-of-principle for using optical emission spectroscopy and artificial neural networks for real-time monitoring and control of the operational parameters of a Hall effect thruster: the anode voltage, the anode xenon injection, the discharge current and the coil current. In that regard, we build an optical database of 26 spectral lines across 6469 operating conditions to train and test the neural network. We then reduced the learning lines from 26 to 15 based on their statistical correlation with the target parameters. After tuning the hyperparameters of the network, the network predicted the thruster's parameters with notable accuracies: 95% for the anode voltage, 84% for the coil current, and 99% for both the anode flow rate and the discharge current. The estimated uncertainty of predictions, at 3σ, is $\pm 51\,\mathrm{V}$ for voltage, $\pm 1\,\mathrm{A}$ for coil current, $\pm 0.15\,\mathrm{A}$ for discharge current, and $\pm 0.15\,\mathrm{mg.s^{-1}}$ for anode flow rate. The predictions calculations were within milliseconds and enabled real-time monitoring of the thruster parameters. Therefore, a PID controller was implemented to regulate the anode voltage and flow rate based on the optical emission of the plume. The PID showcased short settling times from $0.1\,\mathrm{s}$ to $0.4\,\mathrm{s}$ and overshoot levels up to 3% of the target value for the voltage and 10% of the target value for the flow rate. These results were for a fixed coil current at $4\,\mathrm{A}$. The study showed that changing the coil current may necessitate more sophisticated prediction models and control strategies. Future work will expand the model's generalizability to different thruster types, propellants, and magnetic field configurations.

PACS numbers: 0

I. INTRODUCTION

One crucial technology that is currently playing a pivotal role in addressing the increasing market demand for propulsion systems is Hall Effect Thruster (HET). Compared to other electric propulsion solutions, HETs offers advantageous thrust-to-power ratio, specific impulse, total efficiency, lifetime and propellant mass reduction. They have a rich flight heritage[1], ranging from drag compensation and trajectory correction for Low Earth Orbit (LEO) satellites[2] to full orbit transfer for deep space missions[3–5]. HET consist typically of an axisymmetric chamber housing an internal anode and an externally mounted cathode. The propellant is injected at a very low velocity at the anode. Then, a voltage drop is applied establishing an electric field along the symmetry axis. The electric field accelerates the electrons that are emitted by the cathode discharge towards the entrance of the discharge channel. When the electrons reach the latter, they are subject to a strong radial magnetic field produced by external coils which traps them along the magnetic field lines and reduces their mobility. This increases the time spent in the channel and consequently, the probability to produce electron-ion pairs.

Among the diagnostics used to study HET, Optical Emission Spectroscopy (OES) stands out as a promising method for in-orbit monitoring of the thruster[6]. OES has been used in the past to study HET by investigating the electron density and the electron temperature[7–9], the structure of the plume coupled with tomography techniques[10], the evaluation of the rate of the ionization in the channel[11], of the rate of erosion[12,13] and of the plasma kinetics in the thruster's channel[14]. Being non-invasive and easy to implement, it is also widely applied in general in the study of plasma sources for plasma etching and thin-film deposition applications[15–20]. For these applications, OES was integrated not only as a plasma diagnostic but also as a non-invasive control feedback loop to monitor and control the deposition process in a cost-effective manner[17,21]. Meanwhile, the HET community lacks simple control tools that link the emission data to quantitative parameters such as the anode voltage, and the anode mass flow. Yet, this optical footprint is interesting for control purposes and monitoring as it can be more informative than merely taking the voltage and the current as it is usually done during test campaigns. Previous research has focused on predicting thruster performance and control using Machine Learning (ML) models. These models either derive the scaling laws from past thruster designs[22] or predict the discharge current and the cathode voltage to optimize the thruster performance during its operation[23].

Currently, Artificial Intelligence (AI) and ML offer new opportunities for low-temperature

plasma diagnostics and modelling in particular HET research[24] and might be the key to directly infer control parameters of HET from the optical emission. Largely speaking, OES and ML methods have been already used in the fields of material science and chemistry and have demonstrated their capabilities to characterize samples[25,26], recognize patterns[27], and explore molecular designs[28–30] via merely the optical signature of the samples. Implementations of OES and ML are also widely used in plasma etching and plasma-enhanced deposition applications. Indeed, ML and OES were used in particular to monitor and estimate etching parameters[31,32] and also flaws detection for plasma enhanced vapour deposition[33].

In this work, an Artificial Neural Network (ANN) is developed to predict the operating parameters of a laboratory HET, namely the anode voltage, the anode flow rate, the current in the external coils and the discharge current. The idea is to be able to monitor these parameters based simply on the optical footprint of the thruster. A direct application of this ANN is a Proportional-Integrator-Derivative controller (PID) for the anode voltage and flow rate based on the optical emission of the plume that eventually can be embedded in orbit. The optical emission is collected to build a large dataset of operating parameters of a HET. This dataset was subsequently used to train and test an ANN.

This paper is organized as follows. Section II presents the experimental setup, the procedure to collect the dataset and the steps for the development of the ANN. Section III presents and discusses the training and testing results for the prediction of the anode voltage, the anode flow rate, the coil current and the discharge current. Section IV showcases a proof-of-principle for the implementation of a PID controller incorporating the developed ANN to control the anode voltage and anode flow rate. Finally, conclusions are summed up in Section V.

II. THEORY AND METHODS

In the following, we present the experimental setup used to collect the optical emission database followed by the steps for the development of the neural network to predict the operational parameters based on the emission spectra.

A. Experimental setup, data acquisition and cleaning

The emission spectra were collected within the cryogenic vacuum chamber of the PIVOINE 2G[34] test facility in Orléans (France). A laboratory model HET, operating with xenon, was placed inside the stainless steel vacuum chamber, with dimensions of 4 m in length and 2.2 m in diameter. The chamber was maintained at a pumping speed of $70\,000\,\mathrm{L.s^{-1}}$ for xenon, resulting in a background pressure of approximately 5×10^{-6} mbar for a xenon flow rate of $1\,\mathrm{mg.s^{-1}}$. Emission spectra were collected using a collimated optical fibre pointing approximately at $x = 2\,\mathrm{cm}$ from the thruster's exit plane and placed at approximately 1.2 m from the median plane of the thruster, as illustrated in Fig. 1. The optical fibre diameter is 400 µm with a numerical aperture of 0.22. The collimator consisted of a 6 mm diameter lens with an 8.7 mm focal length. This collimator provided an almost cylindrical collection area with a divergence of the field of approximately 0.7 degrees. The collected light from the fibre is then directed to an Avantes $AvaSpec-Dual$ spectrometer[35], designed in a Czerny-Turner setup. The spectrometer has a spectral range from 180 nm to 1060 nm, and uses a blazed-grating optimized for both blue and near-infrared wavelengths. The grating has a density of 600 lines per millimetre and a blaze of 700 nm. The device has a CMOS linear image sensor. It uses a 10 µm slit, providing a resolution at Full Width at Half Maximum between 0.3 to 0.36 nm.

The operating parameters of the thruster (i.e. the anode voltage U_a, the coil current I_b, and the xenon flow rate at the anode q_a) were varied using a LabVIEW interface in the following manner. For a given xenon flow at the anode q_a, the coil current I_b was adjusted by increments of $\delta I_b = 0.2\,\mathrm{A}$, then, for each new value of I_b, the anode voltage U_a followed an increasing ramp within a specified voltage range at increments of 5 V every 0.5 s. At the end of the voltage ramp, the voltage was set to the nominal value of $U_{\mathrm{nom}} = 300\,\mathrm{V}$ before moving to the next I_b value. The xenon flow rate at the anode varied between $1\,\mathrm{mg.s^{-1}}$ and $3.75\,\mathrm{mg.s^{-1}}$, with the cathode flow rate adjusted proportionally. Note that measurements were halted for three to five minutes on average when

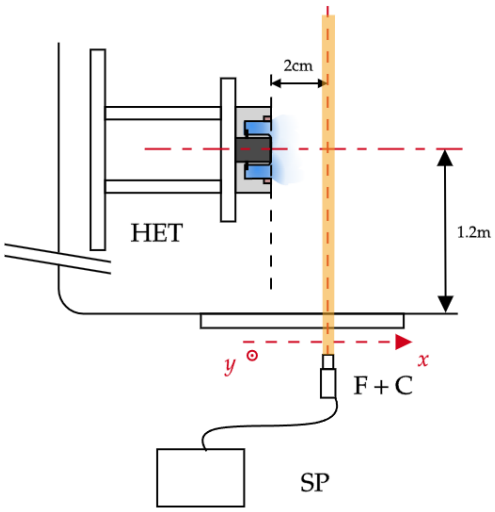

FIG. 1: Schematic of the experimental setup in PIVOINE 2G vacuum chamber. The optical fibre and the collimator are placed at ≈ 1.2 m from the median plane of the thruster and point at the centre of the thruster plume at $x = 2$ cm from the exit plane. SP in the schematic corresponds to the Avantes $AvaSpec - Dual$ spectrometer with a dual channel, allowing to acquire spectra in the 180 nm to 1060 nm. F corresponds to the optical fibre and C to the collimator.

the flow rate was changed to allow the discharge current and the pressure in the vacuum chamber to stabilize before resuming another series of voltage ramps and variations of the coils' current. An example of two measurement cycles is in Fig. 2. Table I sums up the range of the operating parameters explored during the experiment. For each new operating parameter, a spectrum was saved corresponding to the average over eight spectra, each integrated over 25 ms. In addition to U_a, I_b, q_a and the optical emission, the discharge current I_d was monitored during the experiment. Thus, the experiment totaled 6469 spectra, after eliminating redundant points, each corresponding to different state vectors of the thruster (U_a, I_b, q_a, I_d). The effect of hysteresis was not specifically evaluated in this study. The voltage sweep was always in the ascending direction specifically to minimize the hysteresis. The overall findings of this study regarding the implementation of ANN and PID still hold. However, it remains an interesting aspect for further exploration.

Furthermore, the continuous dark background was subtracted from the measured spectra. We then defined a noise threshold of 50 counts corresponding to the maximum amplitude of the remaining signal, and lines with intensities below this threshold were discarded. This ensured a signal-to-noise ratio of at least 2 across the dataset. Moreover, this ensured a consistent set of

TABLE I: The range of the operating conditions of the thruster that was explored during the experiment to build the spectral database.

Parameter	Min	Max	Step
q_a [mg.s^{-1}]	1.00	3.75	0.25
I_b [A]	3.0	5.4	0.2
U_a [V]	200	500	5

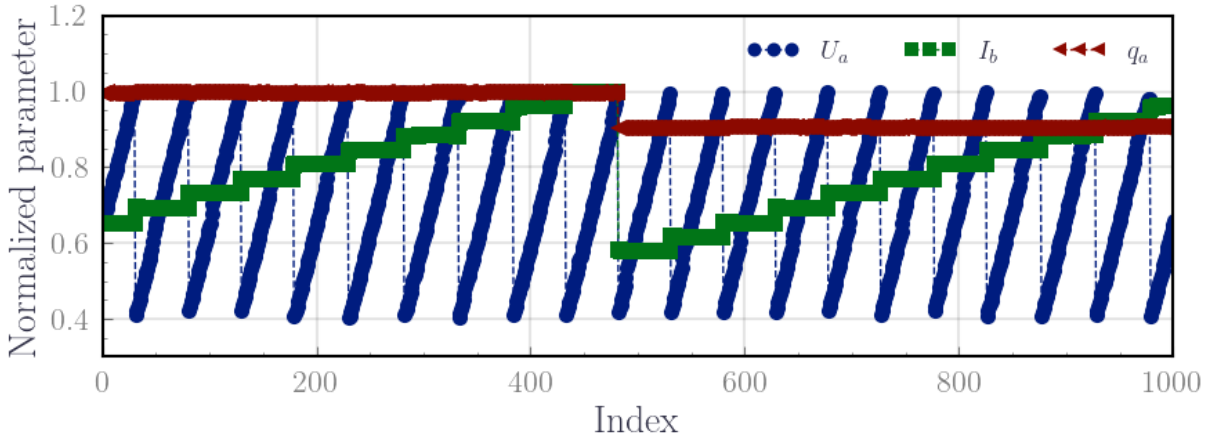

FIG. 2: Example of two measurement cycles. The plot shows the index of the measurement on the x-axis and, on the y-axis, we reported the operating parameter normalized by the maximum values. For a constant flow rate, the coil's current is increased by increments of 0.2 A, and the voltage is varied following an increasing ramp.

lines that were easily identifiable across the dataset from background noise. Line identification was performed manually by comparing the wavelength of the observed peaks in the spectra with the tabulated wavelength list from the National Institute of Standards and Technology (NIST) database[36]. Whenever there was an ambiguity regarding the origin of the spectral line such as whether it was Xe I or Xe II, we considered that the observed line corresponded to the one with the highest tabulated relative intensity in the NIST database. A total of 21 neutral lines and 5 ionic lines were identified. Note that we focused only on the 510 nm to 1060 nm range, based on previous work on collisional radiative modelling of neutral Xe for HET[8,9,14,37] which look primarily into the visible, near infra-red emission:

- Xenon I lines : 688 nm, 712 nm, 728 nm, 733 nm, 758 nm, 764 nm, 788 nm, 797 nm, 820 nm, 823 nm, 826 nm, 828 nm, 834 nm, 841 nm, 882 nm, 895 nm, 904 nm, 916 nm, 951 nm, 980 nm and 992 nm.

- Xenon II lines : 542 nm, 605 nm, 659 nm, 699 nm and 716 nm.

The line intensity was defined as the integral under a fitted Gaussian profile. An example of the fit for the 828 line is given in Fig.3. The spectra were then formatted into an array of 6469×26 intensity lines, each entry corresponding to a distinct operational parameter q_a, I_b, U_a, and I_d. This is the dataset used for the training and testing of the ANN.

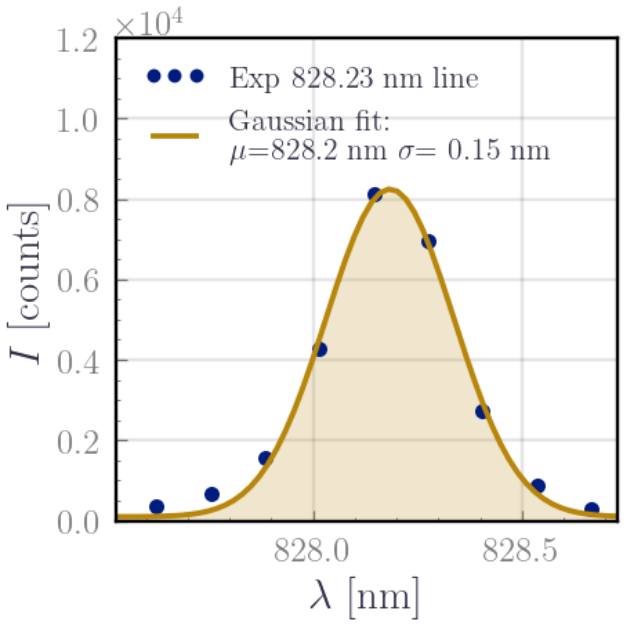

FIG. 3: Example of a Gaussian fit applied to retrieve the line intensity of the 828 nm line from the experimental profile from the spectrometer. The fitted Gaussian function is $f(\lambda) = Ae^{-\frac{(\lambda-\mu)^2}{2\sigma^2}} + c$, where A represents the amplitude of the profile, σ accounts for instrument broadening, and c is an offset accounting for the background signal.

B. Framework and design of the ANN

In this work, we chose to implement a machine learning model using ANNs to predict the state parameters of HET from the collected optical emission spectra of the plume. ANN is designed to mimic the brain structure. It consists of multiple layers of artificial neurons, called perceptron,

that optimize their behaviour through training on large amounts of data to learn complex functions. The model for an artificial neuron is shown in Fig. 4. Typically, the inputs $\mathbf{X} = (x_i)$ are weighed

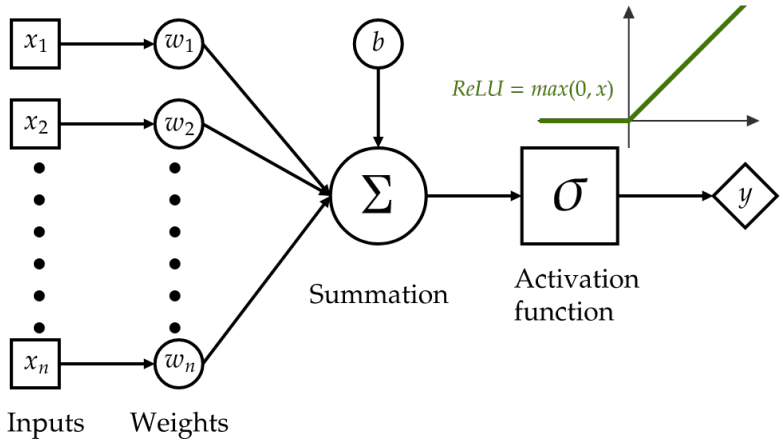

FIG. 4: A representation of an artificial neuron with n inputs x_i. Each input is weighed with w_i and then summed. A bias b is added to the result before passing the result to the activation function σ to yield the output y. The activation function represented on the top right is the Rectified Linear Unit function defined as $\sigma(x) = \max(x, 0)$.

by $\mathbf{w} = (w_i)$ depending on their importance, summed then passed to a non-linear function σ called the activation function to produce the output y. This is represented by the equation:

$$y = \sigma(\mathbf{X}^T \mathbf{w} + b) \ , \tag{1}$$

where $.^T$ is the transpose operator. The output y from one perceptron serves then as an input for multiple other neurons. The perceptrons are organized into different layers thus yielding a network.

Training an ANN consists of iteratively refining the weights w of all the perceptrons to minimize the prediction error on the targets. This is achieved using a gradient descent algorithm where the steepest descent gradient to the weights is calculated using a principle called back-propagation to minimize the cost function/error J. The optimization process can hence be represented as:

$$\mathbf{w}^{i+1} = \mathbf{w}^i - \alpha \nabla_{\mathbf{w}} J(\mathbf{w}) \ , \tag{2}$$

Here, $\mathbf{w}^i$ represents the previous value of the network's weights, $\mathbf{w}^{i+1}$ represents the updated weights, $\nabla_{\mathbf{w}}$ represents the gradient to the network weights calculated using backpropagation, and $J(w)$ represents the error function between the network's output and the target feature.

In practice, the typical workflow for developing an ANN model consists of preparing the data, developing and validating the model via hyperparameters tuning and cross-validation, and finally using the model on unseen data[38]. Here, we used the Scikit-learn library[39] to develop a pipeline for these steps adapted to our application. For each target parameter (anode voltage, anode flow rate, coil current and discharge current), a neural network was developed so that in total 4 ANNs are presented.

The decision to use four separate networks was made for clarity and better interpretability of the error metrics. This approach separates error calculations to avoid unit mismatches and prevent larger parameters from overshadowing smaller ones in the loss function. This is particularly relevant given the disparity between the anode voltage and anode flow rate ranges. The goal was to avoid the model prioritizing error minimization on the largest parameter, which could lead to lower performance on the others. Separating the networks also allows for more straightforward hyperparameter tuning, focusing on optimizing predictions for one parameter at a time. When a single network predicts all four parameters, the strong correlation between them can make it difficult to identify the root cause of underperformance. While we agree that a combined ANN is ideal for deployment and practical use, we prioritized clearer results for analysis. A comparison between the combined and separate ANNs is presented in subsection III.C. In the following subsections, we detail the technical considerations for our application.

1. Preparing the dataset: Feature selection and normalization

First, we reduced the learning spectral lines used to train the ANN by selecting the most "informative" ones out of the 26 lines identified during the experiment. Two metrics were used: the correlation coefficients measured as F-scores and Mutual Information (MI) tests from the Sci-kit learn library. The correlation coefficient quantified the linear dependence of the spectral line intensities and the target variables (q_a, I_b, U_a, I_d). For each spectral line I_i, its correlation coefficient with each target parameter Y_j is computed using:

$$\sigma^2\left(I_i, Y_j\right) = \frac{cov\left(I_i, Y_j\right)}{\sigma_{I_i}\sigma_{Y_j}}\,, \tag{3}$$

Here, $cov(I_i, Y_j)$ represents the covariance between line I_i intensity and target parameter Y_j, while σ_{I_i} and σ_{Y_j} denote the standard deviations of I_i and Y_j respectively. The F-score is derived from

the correlation coefficient as follows:

$$F = \frac{\sigma^2\left(I_i, Y_j\right)}{1-\sigma^2\left(I_i, Y_j\right)} \ , \tag{4}$$

in such a way that a high F score corresponds to a correlation coefficient close to 1 and a low F score corresponds to a correlation coefficient close to 0.

The MI score, on the other hand, measures the information shared between features and target variables and is related to the Shannon entropy[40,41]. High MI scores indicate the importance of a spectral line for predicting the targets. The MI score between variables I_i, Y_j is defined as:

$$I(I_i, Y_j) = \int_{x,y \in I_i \times Y_j} \mu_{I_i,Y_j}(x,y) \log\left(\frac{\mu_{I_i,Y_j}(x,y)}{\mu_{I_i}(x)\mu_{Y_j}(y)}\right) dxdy \ , \tag{5}$$

where $\mu_{X,Y}(x,y)$ is the joint probability distribution and $\mu_X(x)$ and $\mu_Y(y)$ are the marginal probability distributions. This integral was estimated using the nearest neighbour methods[40,41]. Compared to the correlation coefficient, MI is able to strictly detect if two variables are independent or not. Indeed, since the correlation coefficient only detects linear dependencies, the correlation coefficient can be 0 without the variable being independent e.g. for the two random variables X and X^2 where X is symmetric around 0 while The mutual information is non-zero.

These metrics allow us to rank all 26 lines as per their relevance in the prediction of each target feature separately. The results are presented in Section III A. Fifteen lines out of twenty-six were selected to develop the ANN, hence reducing the training time and the risk of overfitting. Finally, the selected lines and target variables were normalised within $[0,1]$ using a Min-Max scaler. We determine the minimum intensity for every emission line and subtract it across all the samples. Then, we divide the result by the difference between the maximum and the minimum values. By doing this, the line ratio, which is usually used along collisional radiative models, is not preserved. Moreover, note that two other scaling methods were tested under the same procedures as explicit in the following paragraphs: scaling by the maximum absolute value and scaling to the normal distribution. This choice didn't have an impact on the learning performance.

2. Hyperparameters tuning and training

The development of the neural network requires tuning its parameters to optimize its predictions of the thruster parameters from the optical emission. The parameters involve the choice of the gradient descent method, the choice of the activation function, the cost functions, the architecture

of the network (i.e. number of layers and number of neurons per layer) and the learning rate value. We used the Adaptive Moment (ADAM) optimization method[42] as it combines the benefits of momentum to smooth out gradients and adaptive learning rates to achieve quick convergence. The ADAM algorithm has three key parameters that require tuning:

- α: The learning rate which controls the step size in the update of the gradients to the weights.
- β_1 and β_2: These coefficients, often close to 1, describe the exponential decay rates for the moving average of past gradients for β_1 and past squared gradients for β_2.

The number of layers varied between 1 and 5 while the number of perceptrons was kept constant across the layers as it should not have a major impact[38]. Moreover, a logistic activation function, a hyperbolic tangent and Rectified Linear Unit (ReLU) were also tested before ultimately selecting the ReLU function since there was no significant impact on the learning performance across the tested functions.

The optimal parameters were determined via a random grid search by exploring the performance of 10000 random combinations of the network parameters and comparing the performance among the tested combinations. Table II lists the ranges of the parameters explored by the random grid search and the probability distribution based on which the values were randomly selected. The models' performance/accuracy was evaluated according to three different metrics:

- R^2 coefficient of determination,
- Mean Squared Error (MSE): $J(\mathbf{w}) = \frac{1}{m}\sum_{i=1}^{m}(y_i - \hat{y}_i)^2$, where y_i represents the target values, $\hat{y}_i$ represents the predicted values, and m is the number of training examples.
- Mean Absolute Error (MAE): $J(\mathbf{w}) = \frac{1}{m}\sum_{i=1}^{m}|y_i - \hat{y}_i|$.

For each tested model during the tuning process, a four-fold cross-validation was performed, as a preliminary validation, for which the dataset was divided into a $2/3$ training set and a $1/3$ testing set.

3. Cross-validations

The model with the best performance from the tuning process was validated using a Monte-Carlo cross-validation[43]. This consists of evaluating the model performance on different training-testing pairs to mitigate the risk of the model performing well on the training data but poorly on

TABLE II: Range of the network parameters explored in the Random Grid Search.

Parameter	α	β_1	β_2	Layers	Perceptrons
Range	$1\times10^{-7}-1\times10^{-2}$	$0.95-0.96$	$0.98-1$	$1-5$	$1-100$
Distribution	Log-uniform	Uniform	Uniform	Uniform	Log-uniform

the testing data. To that end, we performed 10000 random splits of the dataset into $2/3$ allocated for training and $1/3$ for testing. The performance was evaluated using the three metrics specified earlier. The results were plotted into a histogram to inspect the distribution of the model scores across the investigated values. These are presented in Section III.

III. RESULTS AND DISCUSSION

In this section, we present the results from the development of the ANN.

A. Feature selection results

TABLE III: List of the four best-scoring spectral lines based on the F-scores and MI scores for each of the four target parameters. The ionic lines are in bold and the wavelengths are sorted by decreasing F-score.

Parameter	q_a	I_b	I_d	U_d
F-score	**542** nm	788 nm	**542** nm	712 nm
	716 nm	688 nm	**716** nm	980 nm
	605 nm	882 nm	**605** nm	951 nm
	659 nm	828 nm	**659** nm	882 nm
MI score	**542** nm	916 nm	916 nm	980 nm
	916 nm	992 nm	**542** nm	895 nm
	699 nm	904 nm	**699** nm	823 nm
	605 nm	826 nm	992 nm	712 nm

Table III reports separately the four best-scoring lines for each target parameter U_a, q_a, I_d and I_b based on the F-score and MI metrics. The lines, here, are sorted by decreasing value of the reported score.

Interestingly, the best-scoring lines are highly radiative with strong Einstein coefficients. Additionally, all neutral lines, except for the 788 nm and 826 nm, stem from energy levels with a core angular momentum of $j_c = 3/2$, ($2p5 - 2p10$ levels) and corresponds to j_c-preserving transitions. Based on previous work[7,9,14,44], these levels are relevant for OES for HETs to investigate the electron temperature T_e in particular via the use of the 823 nm, 828 nm, 980 nm and 916 nm lines. Here and based on statistical consideration, it is shown that these spectral lines are also correlated with the operation parameters of the thruster. Note also that the ranking is not necessarily the same for different statistical metrics. In particular, for I_b, the best F-scoring lines are amongst the worst scoring MI lines. This reflects that the correlation between the coil current and the line intensity

might require complex learning models.

The F-score results (blue) show that the ionic lines, in particular the 542 nm line, are more informative to q_a and I_d while the neutral lines are more informative to changes in I_b and U_d. Indeed, it is expected that the radiative emission, both from the neutrals and the ions, is dependent on q_a and I_d in such a way that increasing the flow rate leads to enhanced emission in the plume[45]. However, the higher scores of ionic lines against neutral lines to q_a and I_d might reflect their higher sensitivity to the electron temperature when the flow rate changes compared to the neutral lines. On the other hand, the higher score of neutral lines against the ionic lines to I_b and U_d might be attributed to the magnetic field within the HET channel and the ionization source term. Typically we observe a decrease in the neutral lines emission with an increasing voltage and magnetic current. Yet this observation requires further investigation.

Moving forward to the development of the ANN, the learning lines consist of the set of lines reported in Table III except for 659 nm, 716 nm and 951 nm lines. These were excluded from the final selection due to missing diagnostic data in the NIST database. Ergo the learning emission lines consist of 15 spectral lines. It is noteworthy that the reduction in the number of features had no impact on the quality or performance of the learning and testing processes, that are presented in the next section. When comparing models trained on the full and reduced feature sets, no overfitting was observed between the two tests, and the only noticeable difference was the reduction of the training time.

B. Model performance evaluation

Table IV summarizes the best-performing models for each target parameter. Fig. 5 displays the distribution of R^2 scores from cross-validation across 10000 random dataset splits. The developed ANN performs very well, with I_b achieving the lowest R^2 score at approximately 84%, while q_a and I_d models have high scores of around 99%. For q_a and I_d, the linear dependency with the emission intensity accounts for the good performance suggesting that linear models are more adequate to predict these features instead of ANN model. This will be discussed in a further section. Upon examining the error distribution in Fig. 6, both the MAE and the square root of the MSE are small for the four parameters and indicate an average prediction uncertainty between $10\% - 15\%$ in the range of the parameters in Table I. The estimated uncertainty of the prediction at a confidence level of 3σ is ± 51 V for the voltage, ± 1 A for the coil current, ± 0.15 A for the dis-

TABLE IV: Hyperparameters of the best-performing models for each target parameter obtained from the cross-validation results.

	U_a Model	I_d Model	I_b Model	q_a Model
α	3.36×10^{-6}	1.80×10^{-5}	2.51×10^{-4}	8.15×10^{-7}
β_1	0.95472	0.95661	0.95837	0.95792
β_2	0.98549	0.98006	0.99850	0.98145
Hidden layers	4	4	3	3
Perceptrons per layer	90	99	92	92
Initial learning rate	2.42×10^{-3}	2.17×10^{-3}	3.32×10^{-3}	2.38×10^{-3}
R^2 score	$95\% \pm 0.3$	$99\% \pm 0.001$	$84\% \pm 0.05$	$99\% \pm 0.001$

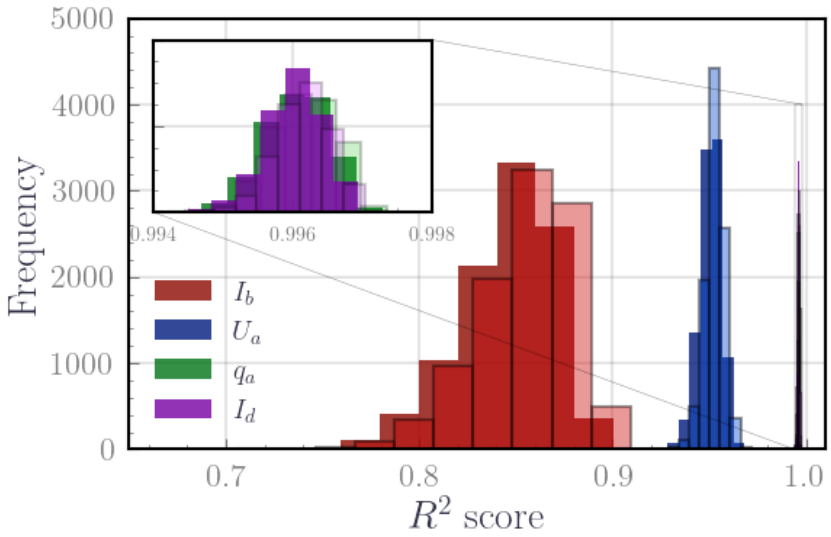

FIG. 5: Distribution of R^2 scores for the selected models for each operation parameter from cross-validation across 10000 models. Opaque colors correspond to test scores when evaluating the model on the test data and transparent color is the training score when evaluating the model on the training data.

charge current, and $\pm 0.15\,\mathrm{mg.s^{-1}}$ for the anode flow rate. For the four parameters, the test score (in opaque colour) and the training score (in transparent colour) are close, highlighting the good generalisability of the model to unseen operating conditions. Fig. 7 shows the predicted vs. target values for U_a, I_b, q_a and I_d. Note that the U_a and I_b present few outliers which explains why the

square root of the MSE for I_b and U_a is twice the MAE while q_a and I_d are close. When inspecting operating conditions corresponding to the outliers, we find out that these points correspond to low anode flow rate conditions $q_a = 1\,\text{mg.s}^{-1}$. The error in the prediction could then be attributed to the reduced reliability of the emission intensity database at low flow rates. Indeed at a low flow rate, the intensity of the emission lines ranges from 500 to 1000 counts compared to high flow rate condition where the intensity of the emission lines range typically from 1000 to 3000 counts, resulting in smaller standard deviations. Consequently, the statistical quality of the learning process might diminish in comparison to high flow rates operations.

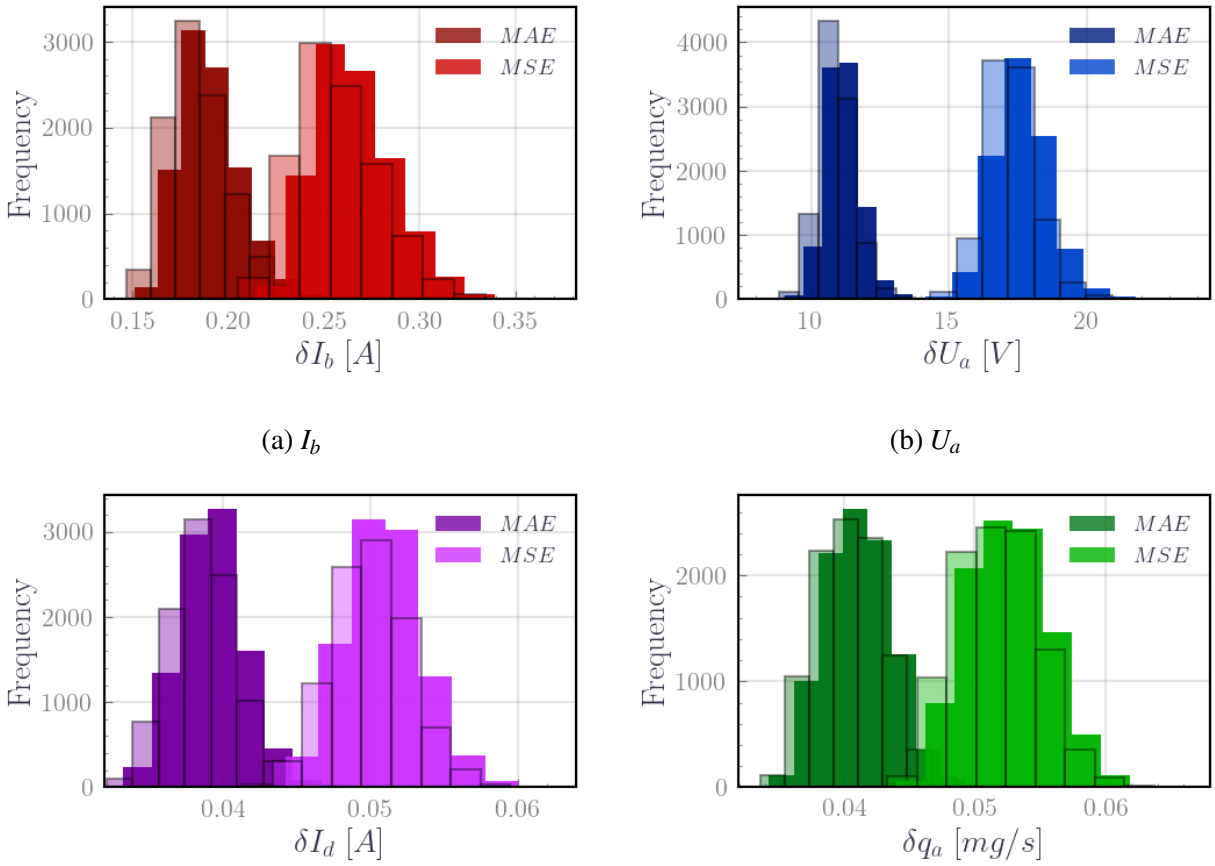

(a) I_b

(b) U_a

(c) I_d

(d) q_a

FIG. 6: Distribution of MAE and the square root of the MSE scores for the selected models for each operation parameter from cross-validation across 10000 models. Opaque colors correspond to test scores when evaluating the model on the test data and transparent color is the training score when evaluating the model on the training data.

All these results give confidence in the ANN to predict U_a, q_a, I_b, I_d from the optical emission

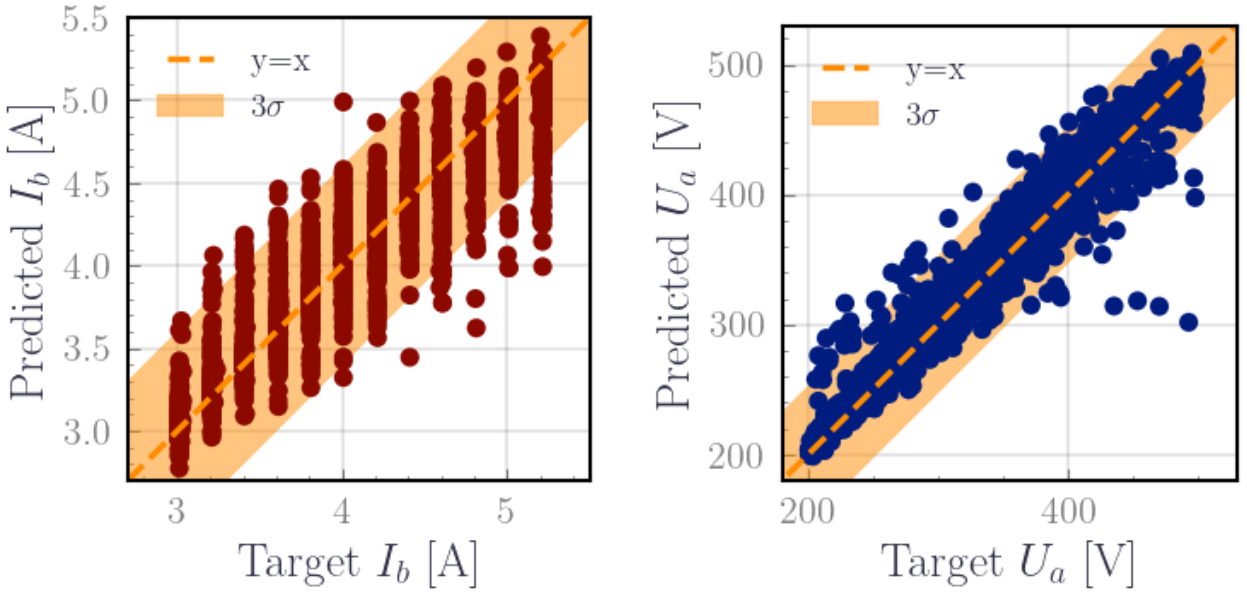

(a) I_b

(b) U_a

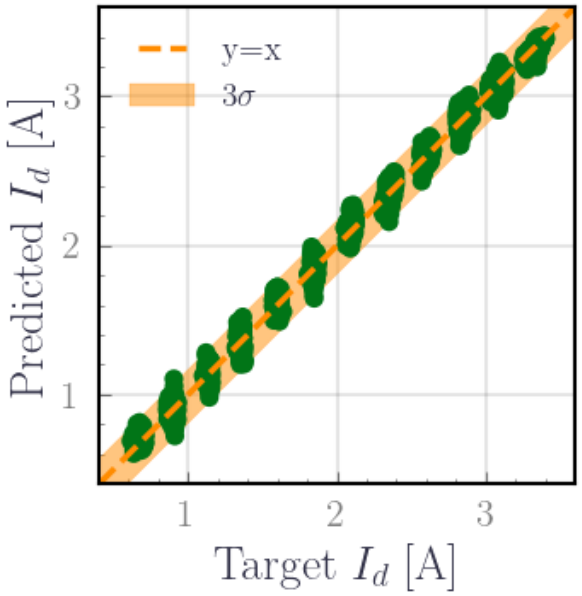

(c) I_d

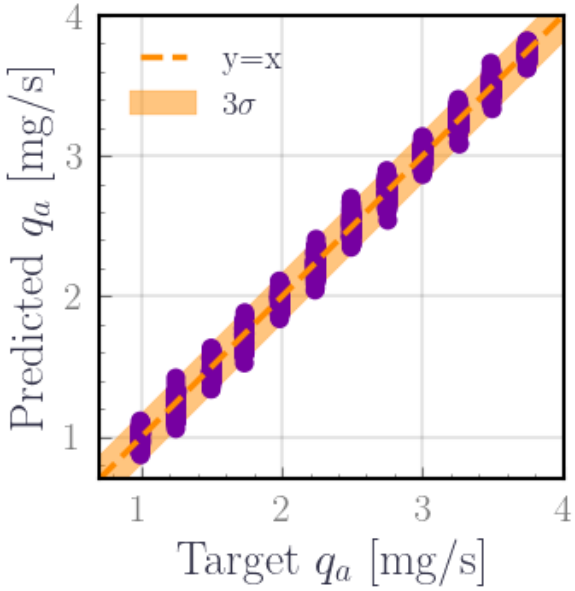

(d) q_a

FIG. 7: Predicted vs. target values for four parameters. The orange line corresponds to the line $y = x$. The predictions align around this line, illustrating the performance of the model. The uncertainty envelope is a 3σ envelope based on the root of the average MSE score.

of the plume. Moreover, the predictions made by the neural networks are fast (a few milliseconds for a single spectrum), which makes it compatible with real-time monitoring of the operational parameters. Finally, it is important to also mention that all 26 lines were used to train the models.

This did not lead to overfitting or any improvement in the performance.

C. ANN vs. other learning models

The almost-perfect score of the ANN on q_a and I_d suggests simpler linear models such as Ridge regression or Lasso might be more suitable. Fig. 8 compares the R^2 scores of three linear models with the developed ANN: linear regression, Lasso, and Ridge regression. The comparison is performed between models that predict each target individually, the results are reported on the first four histograms. The last histogram compares the same learning model types when trained and tested on all the targets simultaneously. The results highlight that the ANN is marginally better than linear models for q_a and I_d, while it outperforms these models for U_a and I_b. Therefore, when aiming for a single model predicting all four parameters simultaneously, ANN outperforms linear models (last bar plot) by being able to accommodate both the linear trends of I_d and q_a and the non-linear trends of U_a and I_b. This concurs with our initial choice of ANN model since it captures better than linear models non-linear trends in the optical emission driven mainly by the electron temperature and the magnetic field.

Moreover, the performance of the combined ANN, as shown in the fifth histogram, mainly reflects the anode voltage due to its high values, as expected. When analyzing also the combined ANN's predictions for each parameter, only marginal improvements on the performance are observed compared to the individual ANNs, with I_b showing again the weakest performance. This highlights that separating into 4 ANN didn't lead to a major improvement in the performance. It also highlights that aggregated score metrics can be misleading and should be interpreted carefully. Separating parameters during model development offers better control and clarity.

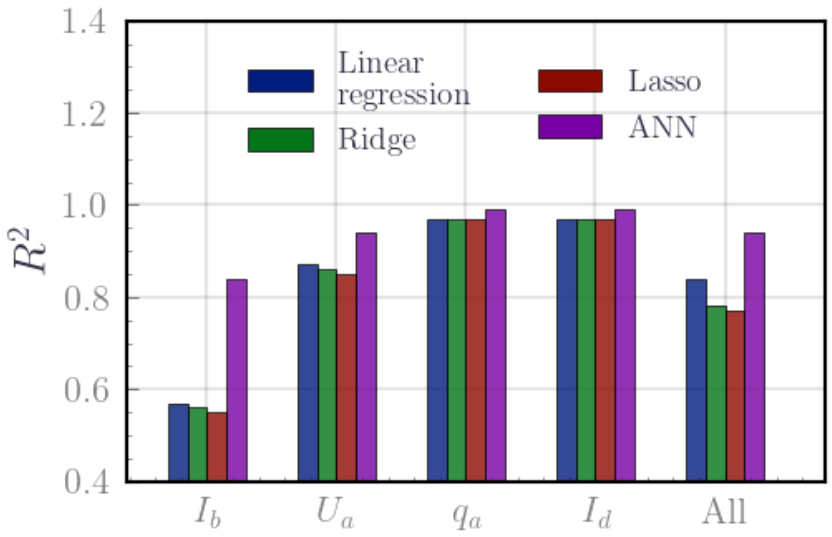

FIG. 8: Comparison of the performance of different linear learning models against ANN. Model performances are grouped by the predicted parameter reflected by the transparency of the bars in the following order: the models predicting I_b then U_a then q_a and finally I_b. The last group of bars corresponds to the models that predict the four parameters at once. The results compare 3 linear models to ANN: Linear regression in blue, Lasso in red, Ridge regression in green and ANN in purple. The plot shows that linear models have a competitive performance on q_a and I_d, while ANN outperforms these models for U_a and I_b.

IV. MACHINE LEARNING CONTROL WITH PID

The previous section showcased how to extract the operating parameters of a laboratory model HET from the emission spectra of the plume, based on a line-of-sight integrated collection of the spectra from a single point. This section presents a proof-of-principle for the implementation of a PID controller with the developed ANN for controlling HETs using the optical emission of the plume based on simulated control scenarios. PID controllers are usually implemented inside the Power Processing Unit (PPU) in HET and are used to control the thrust and the specific impulse during the orbital manoeuvres according to different types of control modes[3,46–52]. Common control modes range from constant thrust and constant power to high specific impulse and high anode efficiency[49].

Specifically, constant power control is typically equivalent to operating the thruster at a constant thrust level. It usually involves changing the gas flow, as it is proportional to the discharge current, complemented with changing the anode voltage as done for instance on SMART-1 mission[3]. In the following, we present a proof-of-principle for the implementation of a similar control strategy with two PID controllers for controlling the flow rate q_a and the voltage U_a using instead the optical emission of the HET's plume and the developed ANN. The proposed control strategy consists of a closed-loop control algorithm, composed of the PID controllers, the thruster and a sensor, which is the spectrometer with the developed ANN (Fig. 9). The control loop involves the following steps:

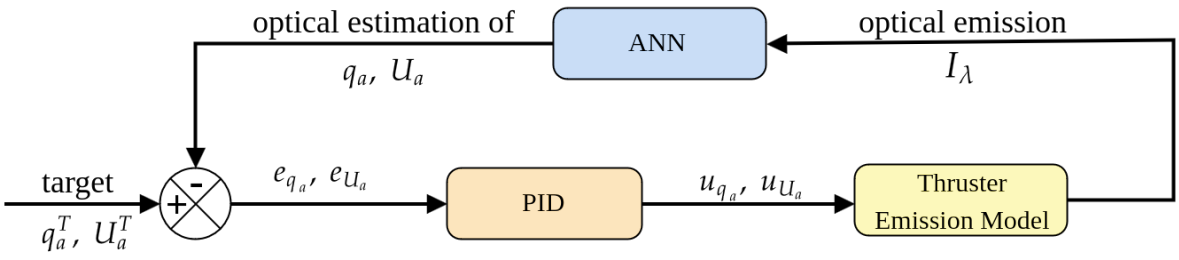

FIG. 9: Block diagram illustrating the closed-loop control strategy: The emission is simulated from the thruster plume and fed into the ANN to estimate the current U_a and q_a. The error e between the target values and the current values is calculated and then fed to the PID controllers to calculate the control action u needed to adjust the voltage and the flow.

1. Set the thruster's target flow and voltage values q_a^T and U_a^T.

2. Estimate the current values of the anode flow rate q_a and the anode voltage U_a from the ANN's prediction from the plume emission spectra.

3. Calculate the error $e_{q_a} = q_a - q_a^T$ and $e_{U_a} = U_a - U_a^T$.

4. Calculate the control action u_{q_a} and u_{U_a} via the PIDs.

5. Adjust the flow and voltage applied to the thruster based on the value of the control actions from step 4.

6. Measure the optical emission from the thruster and repeat step 2 until converging to the target values.

A. Implementation of the PID

PID controllers are widely used in control theory across various industries. They allow to reach a target value for a given system by iteratively adjusting the state parameters through a control action u until the target value is attained and stabilized. The control action u in PIDs aggregates three error components: proportional term (P), integral term (I), and derivative term (D). This is represented mathematically as:

$$u(t) = K_p e(t) + K_i \int_0^t e(\tau) d\tau + K_d \frac{de(t)}{dt} \tag{6}$$

Here, $e(t)$ is the error between current and target values at the instant t, $u(t)$ is the control action, and K_p, K_i, and K_d are the proportional, integral, and derivative gain coefficients, respectively. Two PID were developed in this work, one to control U_a and the second to control q_a. The coefficients K_p, K_i, and K_d for both PIDs are considered constant and were manually adjusted to minimize the rise time and mitigate eventual oscillations using Ziegler's method[53].

In this process, a plasma emission model is required to provide the spectral line intensities from the anode voltage and flow. To that purpose, the plasma emission was determined by linearly interpolating the experimental intensity of the selected spectral lines from section III A over a mesh grid of U_a and q_a for a fixed magnetic configuration. Moreover, Gaussian noise was added to the emission intensities to simulate experimental noise levels. The amplitude peak to peak of the noise was estimated in the experiment to be 50 counts after subtracting the dark. This value

was assumed to correspond to a width of 4σ for the Gaussian noise distribution, i.e. $[-2\sigma, 2\sigma]$, yielding a standard deviation of $\sigma = 12.5$.

Note that a maximum control action u_{max} was included in the controller to prevent the signal from drifting. Specifically, if the calculated control action u is greater than u_{max}, the controller will systematically return u_{max}. The tuned coefficients for the two PID controllers are reported to Table V.

TABLE V: Tuned coefficients of the PID Controller by using Ziegler's method.

	K_p	K_i	K_d	u_{max}
Flow Controller	1	10	1×10^{-3}	$0.5\,\mathrm{mg.s^{-1}}$
Voltage Controller	1	1	5×10^{-5}	100 V

B. Validation of the control

The performance and reliability of the PID controllers were tested on three simulated control cases. The test cases were designed to evaluate both the steady state and step response of the controller by imposing cycles of target values. First, we tested the control of the anode voltage at a fixed anode flow rate. The flow rate at the anode was fixed at $3.5\,\mathrm{mg.s^{-1}}$, with the initial voltage at 280 V. Target anode voltages changed back and forth every 3 s from 250 V to 350 V. The results are shown in Fig. 10a, 10b and 10c. Second, we tested the control of the anode flow rate at a fixed anode voltage. In this case, the voltage at the anode was fixed at 300 V. The initial flow rate was set to $2\,\mathrm{mg.s^{-1}}$, with the target value changing back and forth every 3 s from $1.5\,\mathrm{mg.s^{-1}}$ to $3\,\mathrm{mg.s^{-1}}$. The results are shown in Fig. 10d, 10e and 10f. Finally, we tested the control of the anode voltage and the anode flow rate simultaneously. The initial conditions were fixed at $U_a = 250\,\mathrm{V}$ and $q_a = 1.5\,\mathrm{mg.s^{-1}}$. Five target combinations were tested, again in cycles of 3 s. The target values are explicit in Table VI. They cover cases where reaching the set point requires increasing the voltage with increasing the flow rate, decreasing the voltage with increasing the flow rate, increasing the voltage with decreasing the flow rate and decreasing the voltage with decreasing the flow rate. These cases allow us to assess the PID's robustness to changes in the desired evolution of the target parameters. The results are shown in Fig. 11. In all these simulation cases, the PID controller's frequency was fixed to 100 Hz and the current in the coil was fixed at

4 A.

TABLE VI: The target values for the simultaneous control of q_a and U_a. The initial values were fixed at 250 V and 1.5 mg.s^{-1} then the target values were changed in cycles of 3 s.

Target values	1^{st} cycle	2^{nd} cycle	3^{rd} cycle	4^{th} cycle	5^{th} cycle
q_a [mg.s^{-1}]	2.25	3.00	2.25	1.50	2.25
U_a [V]	350	250	350	250	250

C. Results

The simulation results for the three control simulations illustrate that the outputs closely align with the target values. The solid opaque lines refer to the cases when no noise is introduced, while the solid transparent lines depict the cases where Gaussian noise is introduced. Notably, the control exhibits rapid stabilization, with a minor initial overshoot when transitioning from the initial state to the target set point. Subsequently, the system converges to an error level close to zero, ergo demonstrating a successful implementation of the PID with a virtual ANN optical sensor in simulations at a fixed magnetic configuration with $I_b = 4$ A.

In Fig. 10a, in the case of the voltage control, the PID slightly overshoots between $1-3\%$ from the target voltage value which is equivalent to 6 V. Conversely, in Fig. 10d, in the case of the anode flow rate control, the PID significantly overshoots at approximately 10% from the target flow rate value which is equivalent to 0.3 mg.s^{-1}. This reflects the sensitivity of the optical emission on the flow rate compared to the voltage which has been also noticed during the PID coefficients tuning. Indeed, during this process, the control of the mass flow was particularly sensitive to fluctuations in the emission intensities, hence requiring the flow rate to be adjusted in very small increments and setting a small upper control limit $u_{max} = 0.5$ mg.s^{-1}. In contrast, the anode voltage control demonstrated greater stability, even when larger upper control limits were applied.

The settling time for both the voltage and the flow rate remained relatively small, ranging between 0.25 s to 0.5 s across all control simulations. The settling time for the flow rate was at ≈ 0.5 s on average and is larger compared to the voltage whose settling time was at around ≈ 0.25 s. This reflects again the sensitivity of the emission to changes in the flow rate. Finally, the system exhibited a linear response to noise around the target values which can be limited by averaging the

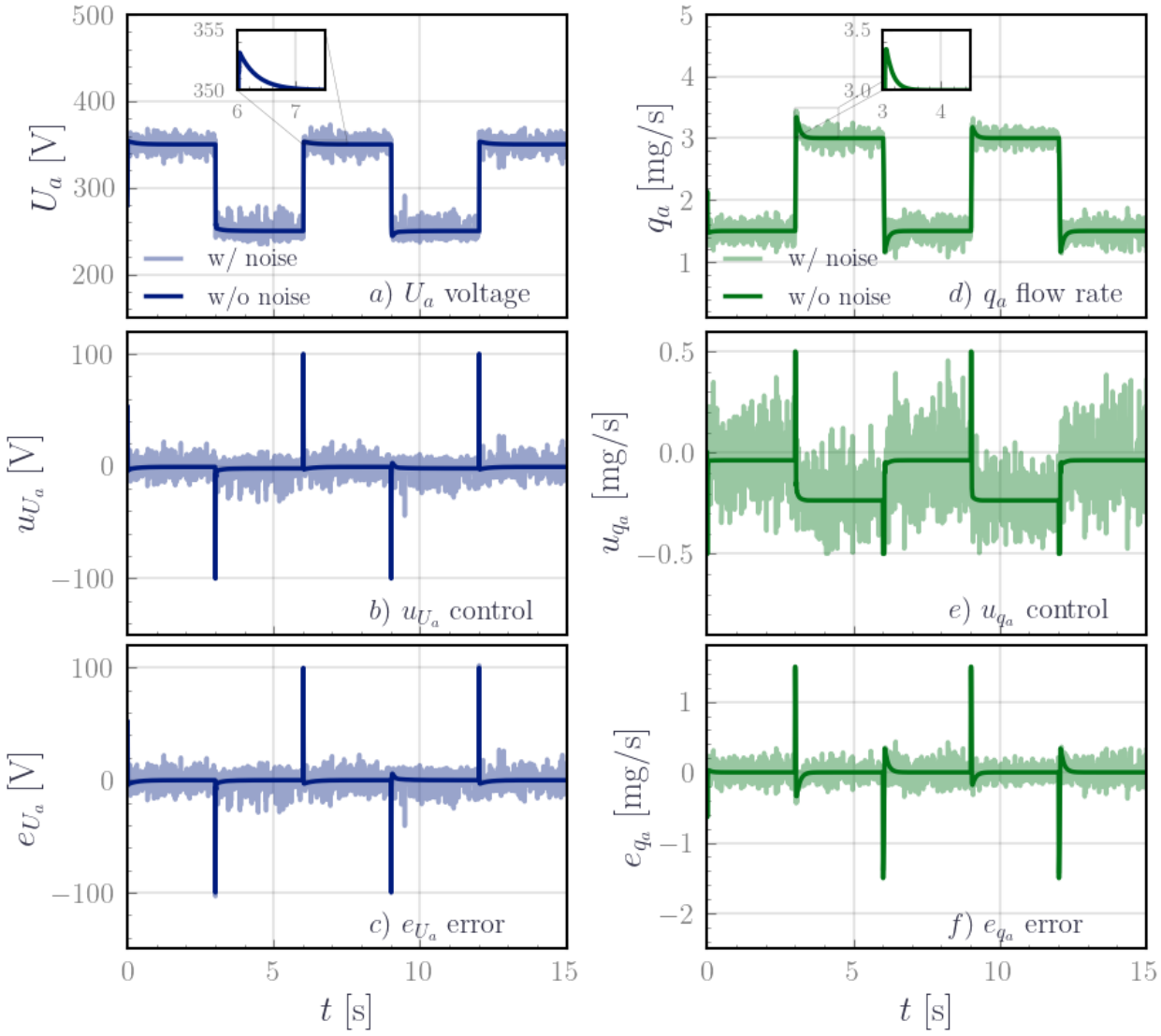

FIG. 10: Control results from the first and second control simulation cases. Panels a), b) and c) are the results of the simulation of the voltage control at a fixed flow rate. The flow rate at the anode is fixed at 3.5 mg.s^{-1}, and the initial voltage at 280 V. Target anode voltages switched every 3 s from 250 V to 350 V. Panels d), e) and f) are the results of the simulation of the flow control at a fixed voltage. The voltage at the anode is fixed at 350 V, and the initial flow rate was set to 2 mg.s^{-1}. Target flow rate switched every 3 s from 1.5 mg.s^{-1} to 3 mg.s^{-1}. From top to bottom, we plotted the controlled parameters, then the applied control action and finally the error between the current and target values.

spectra or by including a lower-band pass filter to the optical sensors to reduce the fluctuations in the emission intensity.

In Fig. 11, in the case of simultaneous control of anode flow rate and voltage, we obtain similarly effective control over the different voltage and flow rate combinations. The settling time ranges between 0.1 s to 0.4 s. The overshoot levels remain comparable to those observed in the previous individual control simulations. However, it is slightly higher for the anode voltage between $1-4\%$ of the target anode voltage. The maximum overshooting occurs in particular when the target voltage is increased to $U_a = 350\,\mathrm{V}$. The overshoot level is 15 V. The settling time in this case is also the longest, at around 0.35 s. When the target voltage is decreased, the PID barely overshoots and settles in less than 0.2 s. For the flow rate, the overshoot levels remain of the order of 10% and don't seem to be dependent on whether the target flow is increasing or decreasing. The minimum settling time is of the order 0.1 s which is achieved at the start of the fourth cycle while the maximum settling time is of the order 0.4 s which is achieved at the start of the second cycle.

D. Control for varied magnetic configurations

The control simulations demonstrated that the PID controller built around the ANN model from Section III can effectively use the optical emission to operate the thruster anode voltage and flow rate. Yet, the coil current was constant throughout the simulation cases, i.e. a fixed magnetic configuration. While this is the typical use case for HET[3,46,49–51], the magnetic configuration can be actively changed to adjust the discharge current[49] or passively modified at the end of life of the thruster due to materials wear. To assess these effects, we slightly change I_b from 4 A to 3.8 A in the third control simulation case. Reported in the Fig. 12 are U_a and q_a results and as expected, the PID controllers perform less efficiently compared to the $I_b = 4\,\mathrm{A}$ condition.

While the overshoot levels and settling time remain relatively unchanged, we observe that the system is unstable with oscillations appearing in the first and third cycles on both the voltage and the flow rate signals. These oscillations are attributed to high values of the proportional gain K_p and they are easily cancelled by reducing the derivative gain K_d. The reason to reduce K_d instead of K_p is because decreasing K_p would directly degrade the settling time. In any case, these observations highlight the need to re-tune the PID coefficients when changing the magnetic configuration. To address this, an adaptative adjustment of the PID coefficients might be achieved for instance with an Adaptive Neural Network PID (ANN-PID) controller[54]. In this case, a neural network would dynamically adjust the PID coefficients in real time based on the system's feedback. This will be the subject of further investigations.

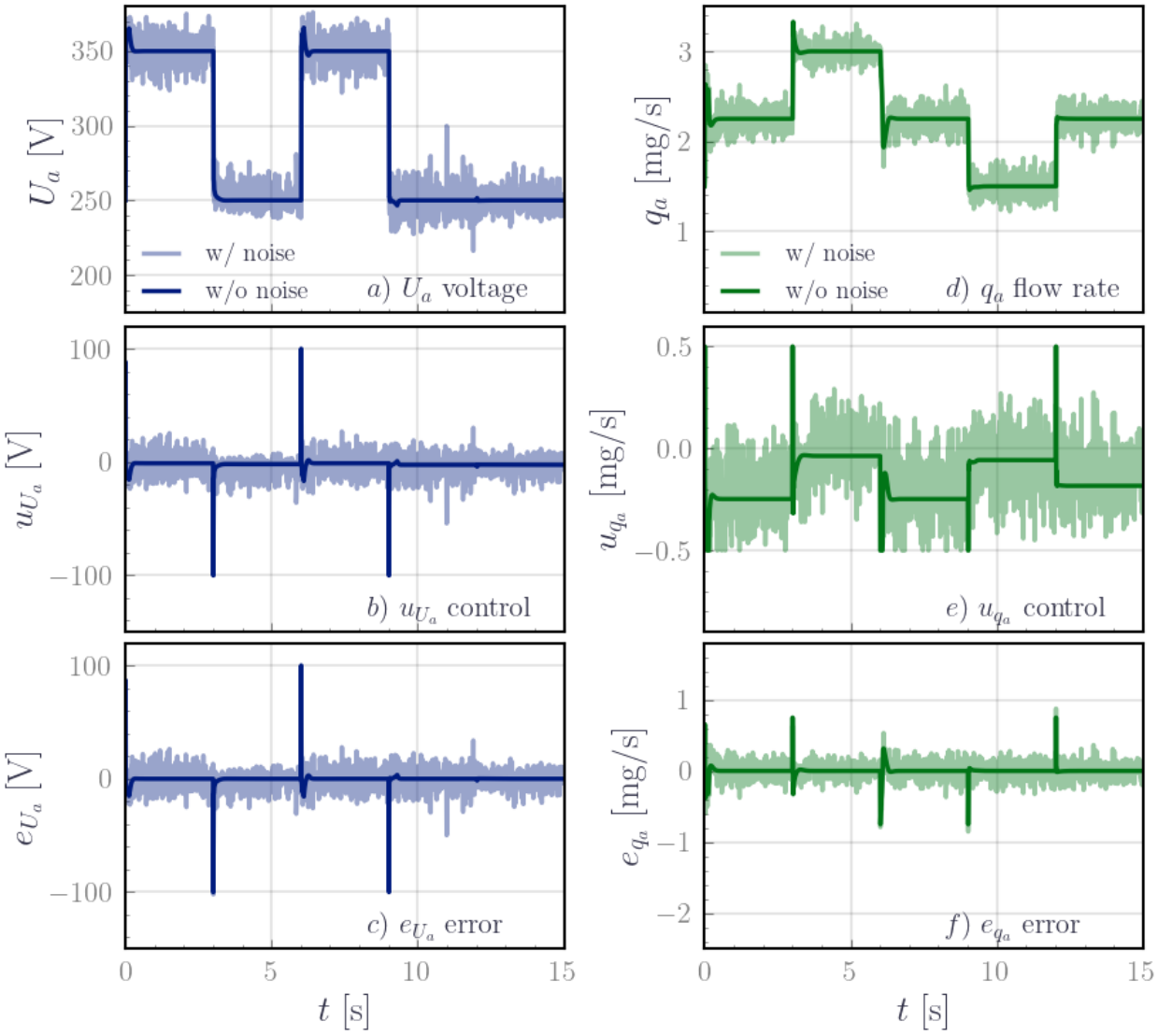

FIG. 11: Control results from the third control simulation case. The initial anode voltage and flow rate are fixed at 250 V and 1.5 mg.s^{-1}. The target values for U_a and q_a are changed every 3 s and follow the cycle explicit in Table VI. From top to bottom, we plotted the controlled parameters, then the applied control action and finally the error between the current and target values.

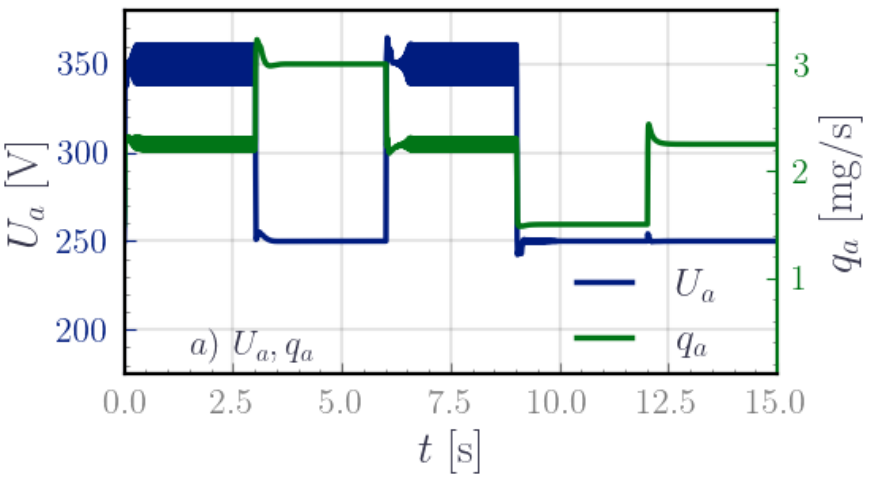

FIG. 12: Impact of changing the magnetic configuration on the stability of the control. The coil current was changed from $I_b = 4\,\mathrm{A}$ to $I_b = 3.8\,\mathrm{A}$. The parameters from the third control simulations are used. The initial anode voltage and flow rate are fixed at 250 V and $1.5\,\mathrm{mg.s^{-1}}$. The target values for U_a and q_a are changed every 3 s and follow the cycle explicit in Table VI. Oscillations appear during the first cycle and the fourth cycle.

V. CONCLUSIONS

In summary, we investigated a method to interface OES with ANN to monitor and control the operating parameters of a laboratory HET. The main advantages of the method are the simplicity and non-invasiveness of the optical data collection and the flexibility and rapidity of the deployment of the ANN to tackle complex features. We demonstrated that the ANN can predict the operating parameters of the thruster to 95% accuracy for the voltage, 84% for the coil current and 99% for the flow rate and the discharge current. The estimated uncertainty of the prediction to 3σ is $\pm 51\,\mathrm{V}$ for the voltage, $\pm 1\,\mathrm{A}$ on the coil current, $\pm 0.15\,\mathrm{A}$ for the discharge current and $\pm 0.15\,\mathrm{mg.s^{-1}}$ for the anode flow rate. The neural network predicts these parameters from the emission spectra collected from a single point in the thruster plume and does not require additional intensity calibration or input compared to traditional OES based inference techniques. Furthermore, the ANN predictions are fast requiring merely a few milliseconds and we demonstrated that this makes it compatible with real-time monitoring and control of the HET. The control strategy consists of a PID and is effective in controlling the anode voltage and flow rate of the thrusters accurately when no change in the magnetic field is expected. The settling time ranged from $0.1\,\mathrm{s}$ to $0.4\,\mathrm{s}$ and the overshoot was at around 3% for the control of the anode voltage and 10% for the control of the anode flow rate. We also showed that changing the magnetic field amplitude by changing the coil's current might require a more sophisticated control strategy. Nevertheless, this proof-of-principle shows promising applications, in the laboratory or orbit. Ongoing work will pursue larger emission ranges to look also into the xenon ion emission in the $400\,\mathrm{nm}$ to $550\,\mathrm{nm}$ and further validation of the optical control method and the impact of eventual hysteresis on the evaluation of the network. The potential for adaptive tuning strategies as the magnetic configurations change is also a promising direction. Practical challenges related to the implementation of the required optics, such as deposition due to the divergence of the plasma plume, stray light correction, and the sensor placement with regards to the thruster, the generalisability to other HET models are a few questions that are currently under investigation before practical implementation of the method. Future research plans to refine the machine learning model to ensure generalisability to other thruster types and propellants and explore alternative control strategies to ensure scalability to changing magnetic field configuration.

ACKNOWLEDGMENTS

This work has been partially funded by ANR (No. ANR-16-CHIN-003–01) and Safran Spacecraft Propulsion within the project POSEIDON. This project has also received funding from the European Union's Horizon 2020 research and innovation programme under grant agreement No. 101004331 (project CHEOPS LOW POWER). Moreover, the authors would like to thank the team of the PIVOINE facility for their welcome and support during the collection of the data, in particular Pascal Lasgorceix and Guillaume Largeau. Finally, the authors would like to thank Federico Petronio and Tsanko V. Tsankov for their support in the revision of the final draft.

AUTHOR DECLARATIONS

Conflict of Interest Statement

The authors have no conflicts to disclose.

Authors Contributions

Tarek Ben Slimane: Conceptualization (lead); Formal analysis (lead); Investigation (equal); Methodology (equal); Visualisation; Writing – original draft (lead); Writing – review & editing (equal). **Alexandre Leduc:** Investigation (equal); Writing – review & editing (equal). **Loic Schiesko:** Investigation (equal); Formal analysis (supporting); Methodology (equal); Writing – review & editing (equal). **Anne Bourdon:** Supervision (equal); Writing – review & editing (equal). **Pascal Chabert:** Supervision (equal); Writing – review & editing (equal).

DATA AVAILABILITY STATEMENT

The data that support the findings of this study are available from Safran Spacecraft Propulsion. Restrictions apply to the availability of these data, which were used under license for this study. Data are available from the authors upon reasonable request and with the permission of Safran Space and Aircraft.

REFERENCES

[1]S. Mazouffre, "Electric propulsion for satellites and spacecraft: established technologies and novel approaches," Plasma Sources Science and Technology **25**, 033002 (2016).

[2]S. Cornara, F. Pirondini, A. Caramagno, M. Price, J. G. del Amo, and B. Carnicero-Domínguez, "Analyses of remote sensing mission scenarios with electric propulsion," in *56th International Astronautical Congress* (2012).

[3]C. Koppel, F. Marchandise, D. Estublier, and L. Jolivet, "The Smart-1 Electric Propulsion Subsystem In Flight Experience," in *40th AIAA/ASME/SAE/ASEE Joint Propulsion Conference and Exhibit* (2004).

[4]J. Jackson, J. Cassady, M. Allen, R. Myers, T. Tofil, D. Herman, and E. Pencil, "Development of high power hall thruster systems to enable the NASA exploration vision," in *Space Propulsion conference* (2018).

[5]J. S. Snyder, V. H. Chaplin, D. M. Goebel, R. R. Hofer, A. L. Ortega, I. G. Mikellides, T. Kerl, G. Lenguito, F. Aghazadeh, and I. Johnson, "Electric propulsion for the Psyche mission: Development activities and status," in *AIAA Propulsion and Energy 2020 Forum* (2020).

[6]W.-J. Zhang, X.-M. Zhu, Y.-F. Wang, G.-X. Wang, Y. Yan, S.-F. Meng, J.-W. Jia, and Z.-X. Ning, "A neural network model relating extraction current characteristics with optical emission spectra for the purpose of a digital twin of miniaturized ion thrusters," Journal of Physics D: Applied Physics **55**, 26LT01 (2022).

[7]G. F. Karabadzhak, Y.-h. Chiu, and R. A. Dressler, "Passive optical diagnostic of Xe propelled Hall thrusters. II. Collisional-radiative model," Journal of Applied Physics **99**, 113305 (2006).

[8]Priti, R. K. Gangwar, and R. Srivastava, "Collisional-radiative model of xenon plasma with calculated electron-impact fine-structure excitation cross-sections," Plasma Sources Sci. Technol. **28**, 025003 (2019).

[9]M. Konopliv, L. K. Johnson, V. H. Chaplin, R. B. Lobbia, A. Thuppul, T. Simka, and R. E. Wirz, "Collisional-Radiative Models of Neutral and Singly-Ionized Xenon in Hall Thrusters: Experimental Validation and Model Investigations," in *AIAA Propulsion and Energy 2021 Forum* (2021).

[10]J. Kim, D. Lee, G. Doh, S. Park, H. Kim, and W. Choe, "Three-dimensional tomographically reconstructed optical emission profiles of hall thruster plasmas," Plasma Sources Science and Technology **31**, 015013 (2022).

[11]Y. Wang, X. Zhu, R. Zou, S. Yan, J. Jia, Z. Ning, and D. Yu, "A novel optical emission spectroscopy method for diagnostics of contribution of different ionization mechanisms and flux of ions in different valences in discharge channel of a Hall thruster," Chinese Journal of Aeronautics (2024).

[12]D. Pagnon, P. Lasgorceix, and M. Touzeau, "Control of the ceramic erosion by optical emission spectroscopy: Results of pps1350-g measurements," in *4th International Spacecraft Propulsion Conference*, ESA Special Publication, Vol. 555 (2004) p. 23.1.

[13]T. Gray, G. Williams, H. Kamhawi, J. Frieman, and I. Mikellides, "Non-intrusive characterization of the wear of the HERMeS thruster using optical emission spectroscopy," (2019), NTRS Document ID: 20190032024 NTRS Research Center: Glenn Research Center (GRC).

[14]X.-M. Zhu, Y.-F. Wang, Y. Wang, D.-R. Yu, O. Zatsarinny, K. Bartschat, T. V. Tsankov, and U. Czarnetzki, "A xenon collisional-radiative model applicable to electric propulsion devices: II. Kinetics of the 6s, 6p, and 5d states of atoms and ions in Hall thrusters," Plasma Sources Sci. Technol. **28**, 105005 (2019).

[15]A. A. Orlikovskii and K. V. Rudenko, "In situ diagnostics of plasma processes in microelectronics: The current status and immediate prospects. part i." Russian Microelectronics **30**, 69–87 (2001).

[16]S. Schiller, U. Heisig, K. Steinfelder, J. Strümpfel, R. Voigt, R. Fendler, and G. Teschner, "On the investigation of d.c. plasmatron discharges by optical emission spectrometry," Thin Solid Films **96**, 235–240 (1982).

[17]K. Bartkowiak, "Direct laser deposition process within spectrographic analysis in situ," Physics Procedia **5**, 623–629 (2010).

[18]L. Song, C. Wang, and J. Mazumder, "Identification of phase transformation using optical emission spectroscopy for direct metal deposition process," in *High Power Laser Materials Processing: Lasers, Beam Delivery, Diagnostics, and Applications*, Vol. 8239 (2012) pp. 120–128.

[19]L. Song and J. Mazumder, "Real Time Cr Measurement Using Optical Emission Spectroscopy During Direct Metal Deposition Process," IEEE Sensors Journal **12**, 958–964 (2012).

[20]C.-L. Chang and F.-C. Yang, "Synthesis and characteristics of nc-WC/a-C:H thin films deposited via a reactive HIPIMS process using optical emission spectrometry feedback control," Surface and Coatings Technology **350**, 1120–1127 (2018).

[21]J. Koo, D. Ha, D. Park, H.-J. Roh, S. Ryu, G.-H. Kim, K. H. Baek, and C. Han, "Design of optical emission spectroscopy based plasma parameter controller for real-time advanced equipment

control," Computers & Chemical Engineering **100**, 38–47 (2017).

[22]Y. Plyashkov, A. A. Shagayda, D. A. Kravchenko, A. S. Lovtsov, and F. Ratnikov, "On scaling of hall-effect thrusters using neural nets," Journal of Propulsion and Power (2022).

[23]K. Ito, N. Yamamoto, and K. Morino, "Sequential prediction of hall thruster performance using echo state network models," Transactions of the Japan Society for Aeronautical and Space Sciences **67**, 1–11 (2024).

[24]J. Trieschmann, L. Vialetto, and T. Gergs, "Review: Machine learning for advancing low-temperature plasma modeling and simulation," Journal of Micro/Nanopatterning, Materials, and Metrology **22**, 041504 (2023).

[25]L. Ward, A. Agrawal, A. Choudhary, and C. Wolverton, "A general-purpose machine learning framework for predicting properties of inorganic materials," npj Computational Materials **2**, 1–7 (2016).

[26]G. Pilania, A. Mannodi-Kanakkithodi, B. P. Uberuaga, R. Ramprasad, J. E. Gubernatis, and T. Lookman, "Machine learning bandgaps of double perovskites," Scientific Reports **6**, 19375 (2016).

[27]J. A. Fine, A. A. Rajasekar, K. P. Jethava, and G. Chopra, "Spectral deep learning for prediction and prospective validation of functional groups," Chemical Science **11**, 4618–4630 (2020).

[28]P. Raccuglia, K. C. Elbert, P. D. F. Adler, C. Falk, M. B. Wenny, A. Mollo, M. Zeller, S. A. Friedler, J. Schrier, and A. J. Norquist, "Machine-learning-assisted materials discovery using failed experiments," Nature **533**, 73–76 (2016).

[29]J. F. Joung, M. Han, J. Hwang, M. Jeong, D. H. Choi, and S. Park, "Deep Learning Optical Spectroscopy Based on Experimental Database: Potential Applications to Molecular Design," JACS Au **1**, 427–438 (2021).

[30]D. Xue, P. V. Balachandran, J. Hogden, J. Theiler, D. Xue, and T. Lookman, "Accelerated search for materials with targeted properties by adaptive design," Nature Communications **7**, 11241 (2016).

[31]R. Shadmehr, D. Angell, P. B. Chou, G. S. Oehrlein, and R. S. Jaffe, en"Principal Component Analysis of Optical Emission Spectroscopy and Mass Spectrometry: Application to Reactive Ion Etch Process Parameter Estimation Using Neural Networks," Journal of The Electrochemical Society **139**, 907 (1992).

[32]S. J. Hong, G. May, and D.-C. Park, "Neural network modeling of reactive ion etching using optical emission spectroscopy data," IEEE Transactions on Semiconductor Manufacturing **16**,

598–608 (2003).

[33]A. Bleakie and D. Djurdjanovic, "Growing Structure Multiple Model System for Quality Estimation in Manufacturing Processes," IEEE Transactions on Semiconductor Manufacturing **29**, 79–97 (2016).

[34]ICARE CNRS, "P.I.V.O.I.N.E. 2G – ICARE – CNRS Orléans," https://icare.cnrs.fr/recherche/moyens-experimentaux/pe-pivoine/ (Accessed 2024-03-25).

[35]Avantes, "Dual-Channel Spectrometers - Avantes | Your Partner In Spectroscopy," https://www.avantes.com/products/spectrometers/starline/dual-channel-spectrometers/ (Accessed 2024-03-26).

[36]A. Kramida, Yu. Ralchenko, J. Reader, and and NIST ASD Team, NIST Atomic Spectra Database (ver. 5.7.1), [Online]. Available: `https://physics.nist.gov/asd` [2020, January 13]. National Institute of Standards and Technology, Gaithersburg, MD. (2019).

[37]G. Karabadzhak, F. Gabdullin, A. Korsun, Y. Plastinin, and E. Tverdokhlebova, "Optical Emission of a Hall Thruster Plume in Space Condition," *the 27th International Electric Propulsion Conference*, (1997).

[38]A. Géron, *Hands-on machine learning with Scikit-Learn, Keras, and TensorFlow: concepts, tools, and techniques to build intelligent systems*, second edition ed. (2019).

[39]F. Pedregosa, G. Varoquaux, A. Gramfort, V. Michel, B. Thirion, O. Grisel, M. Blondel, P. Prettenhofer, R. Weiss, V. Dubourg, J. Vanderplas, A. Passos, D. Cournapeau, M. Brucher, M. Perrot, and E. Duchesnay, "Scikit-learn: Machine learning in Python," Journal of Machine Learning Research **12**, 2825–2830 (2011).

[40]A. Kraskov, H. Stögbauer, and P. Grassberger, "Estimating mutual information," Phys. Rev. E **69**, 066138 (2004).

[41]B. C. Ross, "Mutual information between discrete and continuous data sets," PLoS ONE **9 (2)**, e87357 (2014).

[42]D. P. Kingma and J. Ba, "Adam: A Method for Stochastic Optimization," in *the 3rd International Conference for Learning Representations* (2015).

[43]M. Stone, "Cross-validatory choice and assessment of statistical predictions," Journal of the Royal Statistical Society: Series B **36**, 111–133 (1974).

[44]V. H. Chaplin, M. Konopliv, T. Simka, L. K. Johnson, R. B. Lobbia, and R. E. Wirz, "Insights from collisional-radiative models of neutral and singly-ionized xenon in hall thrusters," in *AIAA Propulsion and Energy Forum* (2021).

[45]K. Hara and I. D.Boyed, "Low frequency oscillation analysis of a hall thruster using a one-dimensional hybrid-direct kinetic simulation," in *the 33rd International Electric Propulsion Conference.* (2013).

[46]E. Bourguignon and S. Fraselle, "Medium Power PPU Activities at Thales Alenia Space in Belgium," in *Proceedings of 37th International Electric Propulsion Conference* (2022).

[47]S. Fraselle and E. Bourguignon, "Low Power PPU Activities at Thales Alenia Space in Belgium," in *Proceedings of 37th International Electric Propulsion Conference* (2022).

[48]E. Trehet, M. Nunez, L. Lecocq, and V. Romero, "Airbus DS Power Processing Units new developments for HET, GIT and technologies status," in *37th International Electric Propulsion Conference* (2022).

[49]Y. Matsunaga, H. Watanabe, S. Cho, I. Funaki, H. Kusawake, K. Kajiwara, F. Kurokawa, and T. Takahashi, "Control algorithm for a 6kW hall thruster," Journal of Electric Propulsion **1**, 29 (2022).

[50]S. Barral, J. Miedzik, and E. Ahedo, "A Model for the Active Control of Low Frequency Oscillations in Hall Thrusters," in *44th AIAA/ASME/SAE/ASEE Joint Propulsion Conference & Exhibit*.

[51]P. Rossetti and D. Valentian, "Analysis of Hall-Effect Thrusters application to formation flying and drag compensation," in *30th International Electric Propulsion Conference* (2007).

[52]M. Leomanni, G. Bianchini, A. Garulli, A. Giannitrapani, and R. Quartullo, "Orbit Control Techniques for Space Debris Removal Missions Using Electric Propulsion," Journal of Guidance, Control, and Dynamics **43**, 1259–1268 (2020).

[53]J. G. Ziegler and N. B. Nichols, "Optimum Settings for Automatic Controllers," Journal of Dynamic Systems, Measurement, and Control **115**, 220–222 (1993).

[54]J. Kang, W. Meng, A. Abraham, and H. Liu, "An adaptive PID neural network for complex nonlinear system control," Neurocomputing **135**, 79–85 (2014).